Cloud height and tracking accuracy of three all sky imager systems for individual clouds

B. Nouri[1], P. Kuhn[1], S. Wilbert[1], N. Hanrieder[1], C. Prahl[1], L. Zarzalejo[2], A. Kazantzidis[3], P. Blanc[4], R. Pitz-Paal[5]

[1]German Aerospace Center (DLR), Institute of Solar Research, Paseo de Almería 73-2, 04001 Almería, Spain

[2]CIEMAT Energy Department – Renewable Energy Division, Av. Complutense 40, 28040 Madrid, Spain

[3]Laboratory of Atmospheric Physics, Department of Physics, University of Patras, 26500 Patras, Greece

[4]MINES ParisTech, 06904 Sophia Antipolis CEDEX, France

[5]DLR, Institute of Solar Research, Linder Höhe, 51147 Cologne, Germany

E-mail: bijan.nouri@dlr.de

Keywords

Nowcasting, 3-D cloud modeling, cloud tracking, cloud height, all sky imager, irradiance map

Abstract

Solar irradiance nowcasts can be derived with sky images from all sky imagers (ASI) by detecting and analyzing transient clouds, which are the main contributor of intra-hour solar irradiance variability. The accuracy of ASI based solar irradiance nowcasting systems depends on various processing steps. Two vital steps are the cloud height detection and cloud tracking. This task is challenging, due to the atmospheric conditions that are often complex, including various cloud layers moving in different directions simultaneously.

This challenge is addressed by detecting and tracking individual clouds. For this, we developed two distinct ASI nowcasting approaches with four or two cameras and a third hybridized approach. These three systems create individual 3-D cloud models with unique attributes including height, position, size, optical properties and motion. This enables us to describe complex multi-layer conditions.

In this paper, derived cloud height and motion vectors are compared with a reference ceilometer (height) and shadow camera system (motion) over a 30 day validation period. The validation data set includes a wide range of cloud heights, cloud motion patterns and atmospheric conditions. Furthermore, limitations of ASI based nowcasting systems due to image resolution and image perspective constrains are discussed.

The most promising system is found to be the hybridized approach. This approach uses four ASIs and a voxel carving based cloud modeling combined with a cloud segmentation independent stereoscopic cloud height and tracking detection. We observed for this approach an overall mean absolute error of 648 m for the height, 1.3 m/s for the cloud speed and 16.2° for the motion direction.

Nomenclature

Symbol	***Definition***	***unit***
Acronym		
ASI	All sky imager	-
CBH	Cloud base height	m
CSP	Concentrated solar thermal power	-
CTH	Cloud top height	m
DNI	Direct normal irradiance	W/m^2
ELM	edge length in meter (pixel orthogonal image)	m/pixel
GHI	Global Horizontal Irradiance	W/m^2
GPS	Global Positioning System	-
MAE	Mean absolute error	x
NWP	Numerical weather prediction models	-
PV	Photovoltaic	-
PSA	Plataforma Solar de Almería	-
RMSE	Root mean square error	x
RSD	Relative standard deviation	%
Latin symbols		
b	Binary orthogonal relative difference images	-
d	Difference images	-
h	Cloud height	m
N	Number of pixel orthogonal image (one axis)	-
o	Orthogonal relative difference images	-
r	Relative difference images	-
t	Time (stamp)	HH:MM:SS
v	Speed	m/s or pixel/s
Greek symbols		
α	pixel elevation angle	°
β	Cloud motion angle	°
θ	Maximum zenith angle orthogonal image	°

1 Introduction

1.1 Motivation for ASI based nowcasting systems

Solar irradiance forecast can be distributed in different temporal resolutions from few seconds to several hours and forecast horizons from several days ahead to intra-day and intra-hour. Different applications require different resolutions and forecast horizons. Nowcasts for the next 15 minutes are beneficial for power plants and grid control. Forecasts with horizons up to several days ahead are needed for unit commitment, scheduling and for improved balance area control performance (**Inman et al. 2013**). Numerical weather prediction models (NWP) provide forecasts up to several days ahead with temporal resolutions in hours (**Lorenz et al. 2009**). More accurate forecasts up to 8-9 h ahead can be achieved by satellite based systems (**Schroedter-Homscheidt et al. 2016**). Due to the spatial and temporal resolution, satellite forecasting systems are not suitable for intra-hour forecasts with sub minute temporal resolution. This gap for the immediate future is closed by ground based all sky imagers (ASI) with a high temporal and spatial resolution (e.g. **Chow et al. 2011**).

Cloud height detection and cloud tracking have a strong impact on the ASI nowcast quality, especially for approaches aiming at spatially resolved irradiance information within an industrial solar field. Cloud heights are decisive for the correct positions of the shadows on the ground. The error of the shadow position on the ground is equal to the error of the detected cloud height in the case of a solar zenith angle of 45°. Furthermore, an erroneous cloud height brings along an erroneous cloud size (**Nguyen et al. 2014**). The influence of the tracking errors on the forecast quality rises with the lead time and leads to false predicted cloud shadow positions. The objective of this work is to improve cloud height detection and cloud tracking of ASI based nowcasting systems.

1.2 State of the art

One approach for nowcasting systems is to introduce additional accurate cloud height and tracking information from supplementary remote sensing systems. Lidars and ceilometers are commonly used to measure cloud height (**Sassen 1991**). Both instruments sample only the sky directly above the sensor. In principle, lidars are capable of measuring cloud boundaries from the cloud base height (CBH) to the cloud top height (CTH) including multiple layers. However, these capabilities are limited due to attenuation of the laser beam, especially for clouds with a high optical depth (**Venema et al. 2000**). This limits lidars often to CBH measurements of the lowest layer. Radar systems like the millimeter-wave cloud radar (MMCR) can scan the entire horizon with a range up to 30 km, measuring different cloud properties such as layer heights, thicknesses, horizontal extent and mean vertical velocity (**Moran et al. 1998**). Both lidar and radar techniques are well established systems but also costly and therefore not suitable for low cost forecasting systems. Comprehensive and continuous coverage of cloud height and motion measurements can be achieved by satellites (**Menzel et al. 1982 & Nieman et al. 1992**). The advantage of satellite based systems is the large field of view. Generally, satellite based systems measure the cloud top height of the highest layer. Some approaches are developed to estimate CBH of the highest layer (**Noh et al. 2017**). However, the temporal and spatial resolution as of today is not suitable for shortest intra-hour forecasts. Currently typical satellite solar nowcasting systems have a spatial resolution with a pixel edge length of 2 to 10 km and a temporal resolution of 15 minutes (**Blanc et al. 2017**). Most advanced next-generation satellite systems, such as the Himiwari-8 and GOES-R, reach a spatial resolution of 0.5 km^2 and a temporal resolution of 10 minutes for Himiwari-8 and 5 minutes for GOES-R (**Bright et al. 2018**). **Bosch & Kleissl 2013** studied the cloud motion estimation with triplets of reference cells and inverter output of a PV solar power plant. This approach might be an alternative for PV power plants, with a forecast limitation defined by the spatial expansion of the solar field.

Due to the financial and technical constraints of low cost forecasting systems, a direct retrieval of cloud height and tracking information from the sky images itself is mandatory. Stereoscopic approaches with two ASIs are frequently described in the literature (**Allmen et al. 1996, Kassianov et al. 2005, Seiz et al. 2007, Nguyen et al 2014, Beekmans et al. 2016, Blanc et al. 2017, Kazantzidis et al., 2017 and Crispel et al. 2017**). Cloud heights are determined by matching segmented clouds from images taken simultaneously by two ASIs. **Peng et al. 2015** developed a similar approach with an additional third ASI. Cloud tracking is achieved in the more recent publications with stereoscopic approaches (starting from **Nguyen et al. 2014**) by block matching with sequentially captured images using cross correlation algorithms.

Quesada-Ruiz et al. 2014 uses a so-called sector-ladder method and a single ASI. Binary images of the sky are overlaid with a sun-centered circular grid. A cross correlation sector matching approach similar to block matching is utilized for cloud tracking. Only clouds moving towards the sun are taken into account for the forecast. **Bone et al. 2018** presented an enhanced sector-ladder system based on the work of **Quesada-Ruiz et al. 2014** with an additional autoregressive filtering. Due to the lack of any cloud height information, the forecast is limited to the vicinity arround the ASI.

Cloud tracking approaches using optical flow instead of the computationally less demanding cross correlation approach are particularly suitable for nowcasting systems working with a singular ASI. **West et al. 2014** developed a system using the dense optical flow algorithm from **Farnebäck et al. 2003**. Similar to the sector-ladder system, this approach lacks any cloud height information and can only derive angular cloud speeds. **Schmidt et al. 2016** and **Richardson et al. 2017** tackle this issue by including additional height information from nearby ceilometers. However, it has to be pointed out that current price of a ceilometer can exceed the price of an ASI by a factor greater than 30 in addition to the limitations due to the point like measurement.

Chow et al. 2015 and **Zaher et al. 2017** conducted comparisons of cloud tracking approaches based on optical flow and cross correlation algorithms. Both conclude that optical flow approaches outperform cross correlation approaches at the price of a greater computational effort. **Huang et al. 2012** proposed a hybrid tracking approach combining the advantages of cross correlation and optical flow approaches.

1.3 Objective of presented work

In this work, the main aim is to optimize ASI based nowcasting by improving the cloud height detection and cloud tracking. The first of three investigated systems is based on a four ASI approach (**Nouri et al. 2017**). The unique feature of this system is that each detected cloud is treated as an individual cloud model with distinct attributes (height, position, surface area, volume, transmittance, motion vector etc.). The image processing is divided into seven processing steps.

1. Clouds are segmented by means of four dimensional clear sky library, accounting for different atmospheric conditions (**Wilbert et al. 2016 and Kuhn et al. 2017a**).
2. Individual cloud models are generated from the segmented camera images by a voxel carving approach (**Nouri et al. 2017**).
3. Each cloud model is tracked individually by comparing 2-D cross sections of the virtual cloud models from sequential image series.

4. Future cloud positions are generated by displacing the cloud models inside the virtual voxel space.
5. Cloud transmittance properties are measured by ground based irradiance measurement stations for DNI and GHI and allocated by a statistical approach.
6. Cloud shadows are projected on a topographical map with ray tracing.
7. Shadow projections are combined with the ground based irradiance measurements and the optical cloud properties to spatial irradiance maps, having edge lengths up to 8 km and resolution down to 5 m.

First validation results for forecasts of 14.5 min ahead showed an overall relative mean absolute error (MAE) of 22.0% for DNI and 18.1% for GHI (**Kuhn et al. 2017a**).

The accuracy of voxel carving based systems depends on the complex cloud segmentation for the cloud height detection (**Calbó et al. 2017 and Kuhn et al. 2017a**). The tracking algorithm compares 2-D cross sections of the virtual cloud models via cross correlation. Thus, segmentation and cloud height errors have a direct impact on the tracking errors. Therefore, a cloud height detection and cloud tracking approach, which is completely independent of the previous processing steps, could improve the systems overall accuracy.

Wang G. et al. 2016 used a cloud height (h) detection method via a known cloud speed in m/s ($v_{m/s}$) measured by a phototransistor based cloud shadow speed sensor (**Fung et al. 2014**) and the angular cloud speed in pixel/s ($v_{pixel/s}$) obtained by an ASI. The cloud height is derived by

$$h = \frac{v_{m/s} \cdot N}{v_{pixel/s} \cdot 2 \cdot tan(\theta)}$$ **Equation 1**

with the maximum zenith angle θ described by N pixel. **Kuhn et al. 2018** adapted this method by obtaining the velocities via two ASI. Two subsequent orthogonal difference images are calculated from a singular ASI and converted into one binary difference image. The angular cloud speed is identified by matching subsequent binary difference images from the same ASI via a normalized 2-D cross correlation. A second ASI is needed to obtain cloud speeds in m/s. Orthogonal difference images from both ASIs are matched. Since the distance between the ASIs is known, the spatial extension per pixel can be calculated. Thus, angular speeds can be linked to absolute speeds.

The method presented by **Kuhn et al. 2018** provides a cloud height and motion information completely independent from previous processing steps but it is limited to one single cloud layer at any given time derived from camera pixels located close to the sun. In this work, we developed a cloud height detection approach, based on the method presented by **Kuhn et al. 2018**, providing individual cloud heights.

Furthermore an additional four ASIs hybrid system is developed, which combines the advantages of the four ASIs voxel carving approach and the two ASI based approach.

In this work, we present the complete system setup with the ASIs and the reference sensors in section 2. Section 3 describes the three distinct 3-D cloud geolocation and cloud tracking approaches. Section 3.1 introduces a four camera voxel carving (4Cam) system, 3.2 a two camera block correlation (2Cam) system and 3.3 a four camera hybrid (4CamH) system. An overview of the main characteristics of the three systems is given in Table 1.

Table 1: Main characteristics of the three ASI based nowcasting approaches

	4Cam (section 3.1)	2Cam (section 3.2)	4CamH (section 3.3)
Number of ASIs used	4	2	4
Detection of cloud height and motion vector depends on cloud segmentation and modeling	yes	no	no
Voxel carving used for cloud modeling	yes	no	yes
Detection of cloud height and motion vector from 3-D voxel space	yes	no	no
Detection of cloud height and motion vector from differential images via a block correlation approach	no	yes	yes

In section 4, we present the results of a 30-days validation period using a reference ceilometer for the cloud height and a reference shadow camera system for the motion vectors (**Kuhn et al. 2017b**). A discussion of our validation results with previously published results is conducted in section 5. Finally, in section 6, we draw the conclusion and present an outlook.

2 System setup

2.1 Configuration of the considered nowcasting systems

The considered systems are located at the Plataforma Solar de Almería (PSA), consisting of three Mobotix Q24 and one Mobotix Q25 standard surveillance cameras as ASIs. All sky images are taken, with fisheye cameras mounted horizontally directed towards the sky. Images are taken every 30 s with a resolution of 3 MP and a fixed exposure time of 320 µs.

All three nowcasting approaches described in this work are real time capable. The image processing computation time varies between 12 to 30 seconds for the 4Cam and 4CamH approach and 6 to 20 seconds for the 2Cam approach. The variations in computation time depend on the prevailing weather conditions. Clear sky and overcast conditions have the lowest and complex multi-layer condition with broken cloud coverage have the highest computing requirements. We use for the image processing the MATLAB® environment. All calculations are performed on a computer with eight Intel® Xeon® E3-1276v3 3.6GHz CPUs and 32 GB memory.

The cameras positions at PSA are depicted in Figure 1. The shortest and longest distances between two ASIs are 495 m (ASI 1 to ASI 2) and 891 m (ASI 1 to ASI 3) respectively.

The inner orientation of the ASIs is determined by a calibration method suitable for fisheye lens cameras introduced by **Scaramuzza et al. 2006**. The outer orientation parameters of the ASIs are described by the geographical position. The GPS and altitude information used for the outer orientation are measured directly by a handheld GPS receiver. The misalignment of the cameras between the optical axis and the zenith is determined by tracking the full moon in camera images at nighttime. Three tilt angles are identified iteratively by minimizing the root mean square deviation between the detected moon positions and the expected moon position of an ideally mounted camera.

A virtual voxel space with a horizontal edge length >20 km, a height of 12 km and a resolution of 50 m is generated. This space is created around a point of origin roughly in the center of the four cameras (see Figure 1). Each camera pixel can be described as a vector through the voxel space. This space serves as a coordinate system for the cloud models in all three approaches.

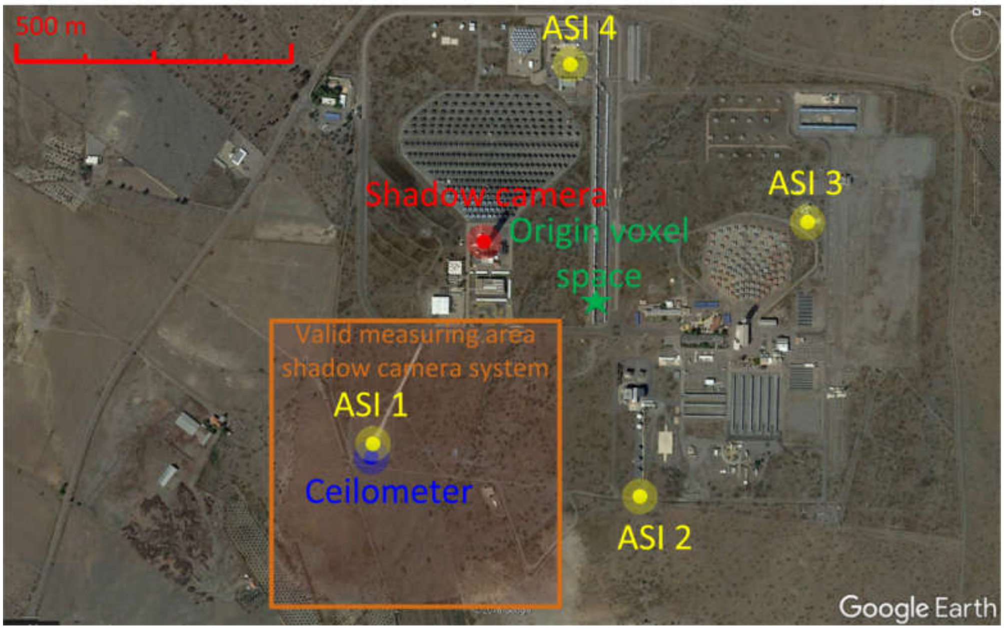

Figure 1: Aerial image of PSA with markers for the camera positions and reference systems as well as the point of origin of the used coordinate systems. The orange frame indicates the valid measuring area of the shadow camera system, in which cloud shadow speeds are determined (Source: Google Earth [Accessed: 05.05.2018]).

2.2 Reference cloud height measurement system

A CHM 15k Nimbus ceilometer from the G. Lufft Mess- und Regeltechnik GmbH is positioned 7 m south to the ASI 1 position in the southwest corner of the PSA (see Figure 1). The CHM 15k is capable of measuring simultaneously multiple cloud layers. However, the attenuation of the laser beam within clouds, limits the multi-layer capabilities to clouds with a cloud optical thickness below 3 (**Venema et al. 2000**). The global cloud optical thickness average for low-level clouds (cumulus, stratocumulus and stratus) is around 4.7 (**Rossow & Schiffer 1999**). Therefore, we use in this work only the CBH measurement of the lowest cloud layer, as detected by the ceilometer.

Despite the detected average bias of 160 m between the CHM 15k and a CL31 Vaisala ceilometer by **Martucci et al. 2010**, we consider the accuracy of the CHM 15k sufficiently as a reference system for the ASI based nowcasting systems.

2.3 Reference cloud motion vector measurement system

As reference for cloud motion we use a so-called shadow camera. This shadow camera is mounted at the top of an 87 m solar tower, taking ground images. Shadows on the ground are detected and tracked. **Kuhn et al. 2017b** developed this novel cloud (shadow) motion vector measurement device and used it to benchmark a Cloud Shadow Speed sensor (**Fung et al. 2013**). The benchmarking study observed a root mean square error (RMSE) of 2.69 m/s, MAE of 1.61 m/s and a bias of 0.20 m/s over a 59-days test period between the shadow camera and the shadow speed sensor. The shadow camera system observes an area south of the solar tower (see Figure 1). The measuring area has an edge length of 525 m. Images are taken with a temporal resolution of 15 s. The geometrical size and temporal resolution limits the shadow camera system to speeds up to 17.5 m/s. For speeds up to this limit, the shadow edge of an incoming cloud is detected in two subsequent images, even in the case of a cloud path orthogonal to the borders of the measuring area.

3 Individual cloud modeling and tracking

3.1 Four camera voxel carving based system

This section summarizes the 4Cam system. A more detailed description of the 4Cam system is given in **Nouri et al. 2017**.

3.1.1 Cloud modeling with voxel carving

Each camera pixel corresponds to an array of voxels, describing the line of sight from the camera lens to a voxel space border. Binary images created by the segmentation, identify the cloudy pixels. The 4Cam system takes the cloudy pixels and marks all corresponding voxel as a cloud. Each of the segmented images would individually result in a voxel space with cone shaped clouds, starting from the cameras position. A more precise cloud shape is achieved by the cross sections of the four generated voxel spaces (**Kutulakos et al. 2000**). All cloudy voxels, connected with each other are aggregated and describe individual 3-D cloud models. Due to the size of the voxel space with an edge length >20 km (horizontal plane) and the positions of the ASI bundled around the voxel space origin (average distance ASIs to origin around 420 m), only minor deviations of the viewing angles exist between the cameras to most of the clouds. Thus, in many cases, the detected cloud models maintain their cone shape (see Figure 2 on the left). Subsequent cloud height detection and final modeling processing steps are needed.

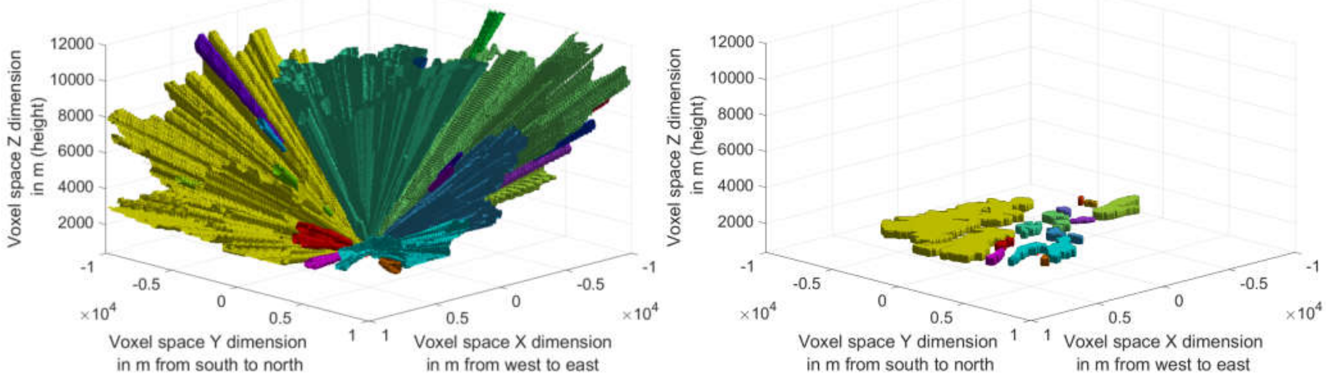

Figure 2: Cloud models in voxel space (each color represents an individual cloud models) left) before height detection and final modeling right) after height detection and final modeling (relevant for 4Cam and 4CamH)

The cloud height determination is presented in Figure 3. The widest horizontal voxel layer approximates a position closely beneath the cloud center height, for small cloud models positioned in the center of the field of view of several ASIs (Figure 3 (a)). For the remaining cloud models, the cloud height can be determined by the intersection of the field of views at the cloud model edges. The cloud edges are described by the corresponding minimum and maximum pixel elevation angle ($\alpha_{min/max}$) of a cloud cross section (see Figure 3 (b and c)). Each side of large cloud models, which is partially above the point of origin, is treated separately. The cloud edges are detected by the minimum pixel elevation angles corresponding to pixels located at the same side. Four cameras result in six intersections for each cloud edge and therefore in twelve cloud height values for two cloud edges. The derived cloud height is not the CBH, but a center height determined as the average of all measurements.

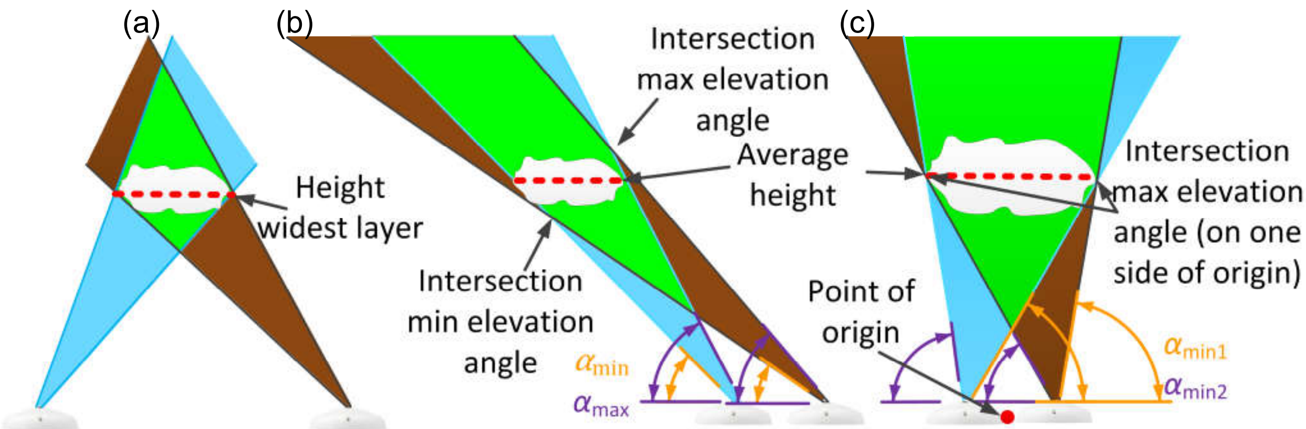

Figure 3: Three distinct cases for cloud height detection from voxel space. (a) 2-D depiction of a small cloud inside the voxel space positioned between the cameras (widest voxel space layer corresponds to cloud height). (b) 2-D depiction of cloud inside the voxel space positioned at the outskirts of the field of view of several cameras (line of sight

intersections of several cameras at the cloud edges correspond roughly to the cloud height). (c) 2-D depiction of large cloud inside the voxel space positioned at the center of the field of view of several cameras (intersection line of sight of several cameras at the cloud edges corresponds to cloud height) (relevant for 4Cam)

Some information about the cloud thickness is retrieved with multiple ASIs, but the accuracy of these readings depend strongly on the relative cloud position, size and height. Therefore, we introduce a simplified cloud thickness estimation. The cloud thickness is related to the cloud type (**Wang&Sassen 2001**). The occurrence of cloud types is connected to the cloud height (**Kahn et al. 2008**). We estimate the geometrical cloud thickness as a function of the retrieved cloud center height, with a decreasing thickness while increasing cloud height. The cloud thickness estimations are chosen according to the global cloud thickness frequency distribution published by **Wang 2000**. We do not consider vertical variability of the geometrical height inside a single cloud model. It is clear that this estimation will struggle in the case of very thick clouds, such as nimbostratus or deep convective clouds. During conditions with such clouds, the size and distribution of the projected cloud shadows on the ground will be underestimated. However, these cloud types can be associated often with rainy overcast conditions (**Wang&Sassen 2001**), without significant shadow-free spaces on the ground. Especially, considering the relatively small areas covered by the nowcasting system (edge lengths up to 8 km). Thus, in such conditions the irradiance forecast quality is mainly affected by the determined cloud radiative effect and not by the determined cloud height or cloud motion. It should also be taken into account, that the cloud optical thickness of nimbostratus or deep convective clouds is above 23 (**Rossow & Schiffer 1999**), and therefore only low irradiance and no or little power generation is found in such cases.

Increased uncertainties arise from clouds that are located partially or completely outside the voxel space and/or due to segmentation uncertainties. The relative standard deviation (RSD) between the twelve distinct cloud height values (six per cloud edge) will rise in cases with increased uncertainties. Average cloud height information with a low RSD ($RSD \leq 5\%$) are considered as trustworthy and saved into a short-lived database (only data from the same day). Cloud height information from cloud models with an RSD above a certain threshold value ($RSD \geq 12.5\%$) are rejected. These cloud models receive cloud height information from the database preprocessed by a Kalman filter (**Kalman 1960**). The RSD thresholds are defined based on the authors' experience and first preliminary validation results. This approach will fail during fully overcast conditions. However, fully overcast conditions make cloud height information irrelevant for the creation of the irradiance maps.

3.1.2 Cloud tracking with voxel carving

Horizontal 2-D projections of all 3-D clouds taken at the cloud center from the current image set are compared via a cross correlation algorithm to the 2-D projections of the cloud models from the previous image set. Matches are rejected due to significant deviations in cloud heights or unrealistic high cloud speeds. Motion vectors are derived from matches. Segmentation and 3-D modeling errors increase for clouds located closer to the image horizon. For these cloud models direct tracking is not feasible. Motion vectors derived from clouds located close to the image zenith (zenith angle 35°) are allocated to those clouds. All valid motion vectors are saved together with the corresponding cloud height into a database. Motion vectors for all cloud models without valid motion vectors are calculated from the database via a Kalman filter, considering only the database entries from clouds of the same day and height range.

3.2 Two camera block correlation system

Figure 4 illustrates the 2Cam cloud height determination and tracking approach. Both height detection and tracking are based on the same three-step strategy. Where the height determination uses two subsequent images of two distinct ASIs, the tracking uses three subsequent images of the same ASI without the third step. The goal of this approach is to create orthogonal height and motion maps for the cameras. Orthogonal images are created according to **Luhmann 2003**. The matching process illustrated in step 2 of Figure 4 is done by a block matching cross correlation algorithm. For both applications the block discretization is defined by the detected average cloud height from the previous time stamps. Higher clouds result in smaller pixel displacement at the same cloud speed. Thus, the matching of motion via cross correlation gets more error prone with higher clouds. Larger blocks and consequently larger search areas address this challenge but reduce the capabilities of identifying distinct cloud layers.

The original approach from **Kuhn et al. 2018** derives a single height and speed information at any given time stamp for the entire sky, based only on the camera pixels close to the sun. The approach presented here derives distinct cloud height and cloud speed information for each pixel of the camera image.

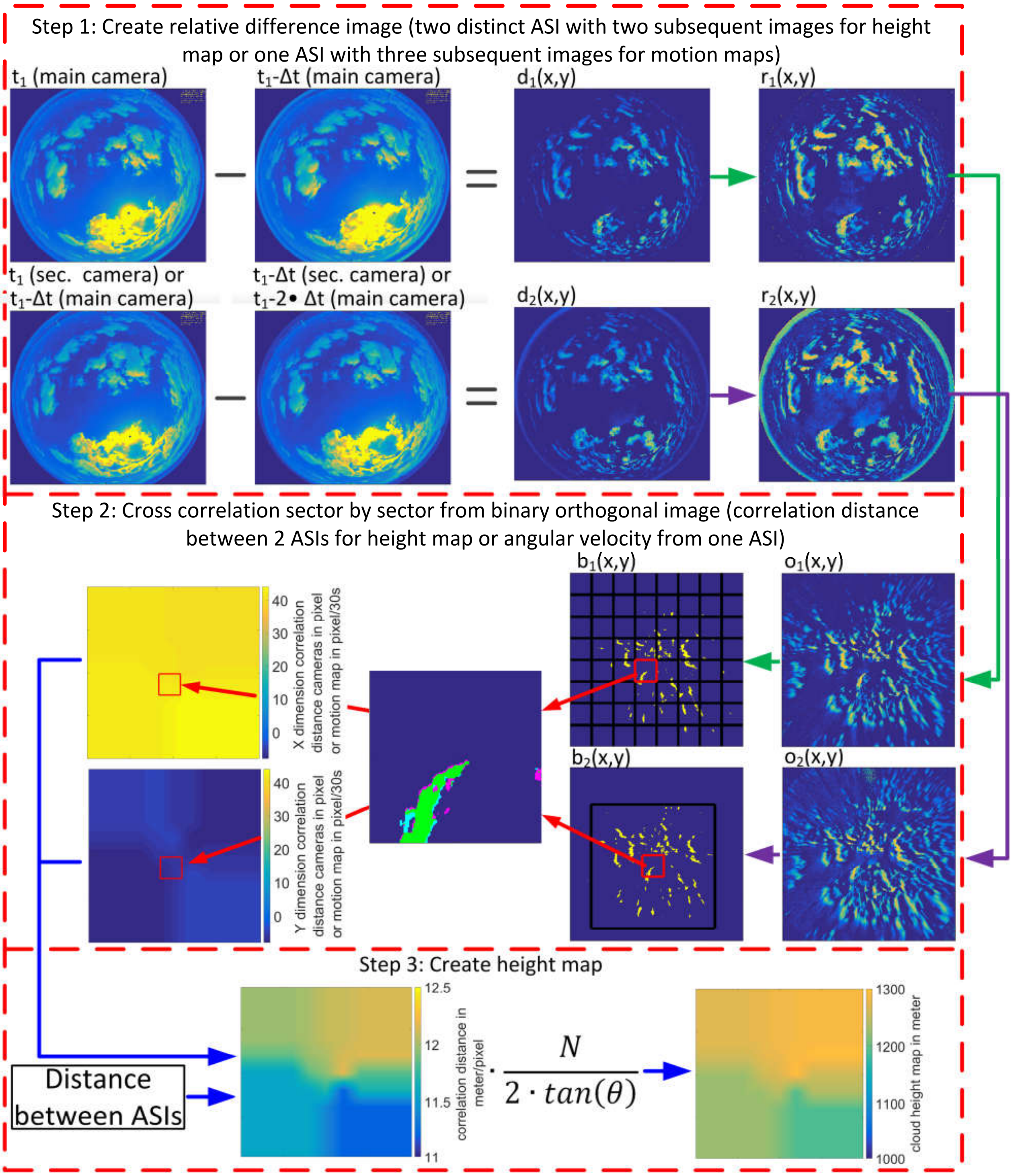

Figure 4: Creating motion maps (step 1 and step 2 with one ASI and three subsequent images) or create height map (step 1, step 2 and step 3 with two ASIs and two subsequent images). Step 1: Calculating difference images from the red channel of subsequent images ($d_i(x,y)$) and convert difference images into relative difference images ($r_i(x,y)$). Step 2: Create orthogonal relative difference images ($o_i(x,y)$). The orthogonal images are converted by variable thresholds into binary images ($b_i(x,y)$). Motion maps in pixel/30 s (one ASI with three subsequent images) or correlation distance maps in pixel (two ASI with two subsequent images) for both horizontal dimensions are created via cross correlation (block by block). Step 3: Under consideration of the distance between the ASIs and the correlation distance maps, the edge length in meter is known for each pixel. Finally, the cloud height map can be calculated with some geometrical informations of the orthogonal images (maximum zenith angle θ and the diameter N defined by θ in pixel). (relevant for 2Cam and 4CamH)

Cloud heights are derived as long as motion is detected in the sky, which enables cloud height detections during overcast conditions. One minute average values are created for the height and motion maps.

The determined cloud height corresponds to an average cloud center height and not to the CBH. The approach described in section 3.1 is used again to define the geometrical cloud thickness.

Segmentation results are not needed to derive height and motion information, but required for the cloud-modeling step. The cloud height map is overlaid with an orthogonal segmented image (see Figure 5). Thus, the cloud height for each pixel identified as cloudy as well its estimated geometrical thickness is derived.

The transfer of the cloud information from the orthogonal image to the 3-D voxel space is done layer by layer. The resulting edge length in meter (ELM) from the corresponding pixels of the orthogonal image is calculated according to Equation 2.

$$ELM = \frac{tan(\theta) \cdot h \cdot 2}{N}$$ **Equation 2**

The known position of the camera inside the voxel space and the pixel ELM, enable us to match each cloudy pixel to a single voxel of the corresponding voxel space layer. The geometrical thickness of the cloud is taken into account, by marking the corresponding voxels from layers above and below.

Segmentation errors have an influence on the 3-D cloud model shape and size. The influence of such segmentation errors is reduced by utilizing the segmentation results of the secondary camera. Voxel remain marked as cloud, only if the corresponding pixel from the secondary camera is segmented as cloud.

The same match from the orthogonal cloud height map is used also for the orthogonal motion map. Thus, each voxel marked as cloud gets a motion vector from the orthogonal motion map.

Individual 3-D cloud models are identified by grouping all connected cloudy voxels. An average motion vector is calculated from the velocities allocated to each voxel within a single 3-D cloud model. These average motion vectors are saved with an expiration date (12 hours) together with the corresponding average cloud height into a database. The motion vectors of the database are processed with a Kalman filter, treating datasets from different height layers separately. The

Kalman filter weights more recent measurements stronger, and thus reacts fast when the conditions change. Older measurements have only a notable effect after longer clear sky periods. The filtered motion vectors are allocated to the 3-D cloud models according to the average cloud height.

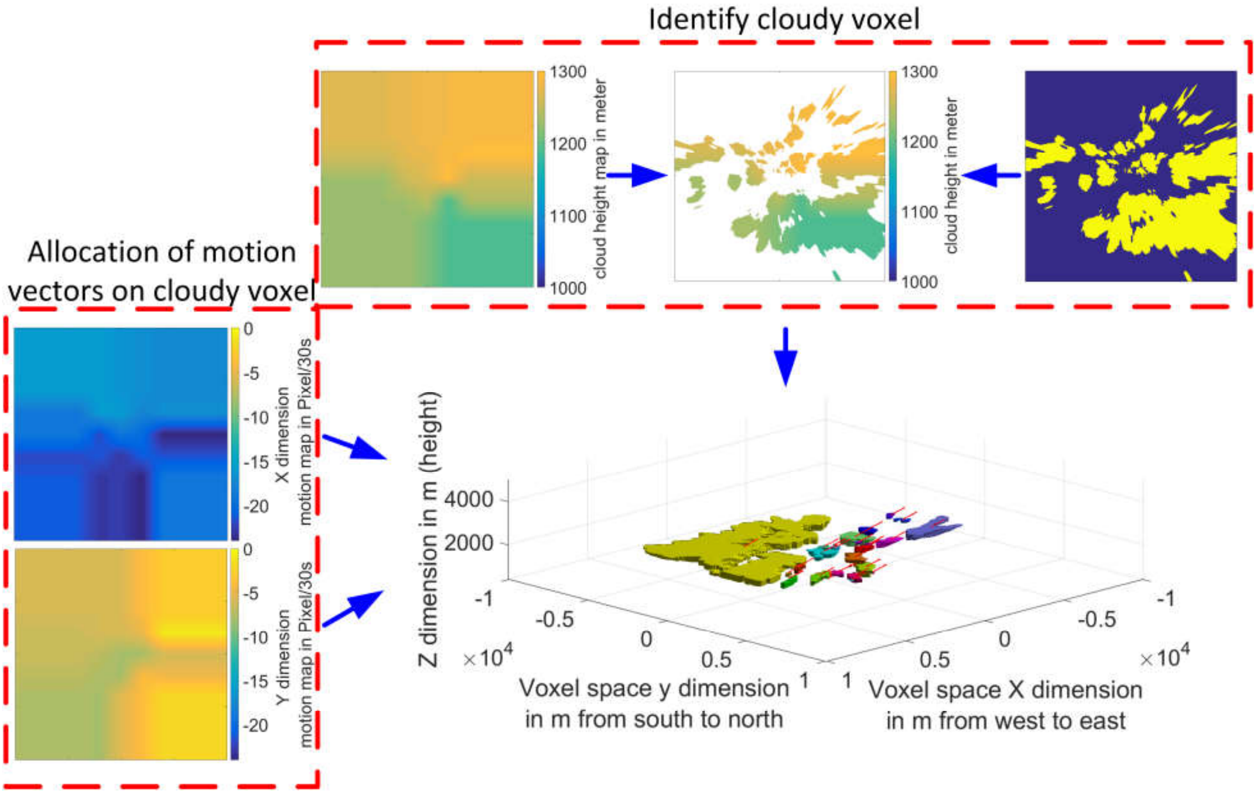

Figure 5: Height map overlaid with binary segmentation image. Coordinate transformation from 2-D orthogonal image with height information to 3-D voxel space (each color represents an individual cloud model). Allocate speed vectors from 2-D orthogonal motion maps to cloudy voxels (relevant for 2Cam)

3.3 Four camera hybrid system

The 4CamH system is a hybridized approach, which uses voxel carving cloud modeling combined with the height detection and tracking approach of the 2Cam system.

Four cameras allow six distinct ASI pairs. Due to the limitations of processing time for real-time nowcasting systems, the number of used pairs is reduced to four. In this work we used the following pairs (first main camera, see Figure 1):

- ASI 1 → ASI 2
- ASI 2 → ASI 3
- ASI 3 → ASI 4

- ASI 4 → ASI 1

Each pair generates separate cloud height maps and motion maps using the processing steps described in section 3.2. The four sets of motion and height maps are inspected for any strong deviations from the average (>20%). The used threshold is based on the authors experienced and first preliminary validation results. If necessary, individual maps are rejected and the remaining maps are averaged. Increasing the amount of used ASI pairs to five or six would increase the redundancy of the cloud height and motion information. However, it is unlikely that all four currently used ASIs pairs are rejected at the same time (never experienced by authors). Thus, no significant overall improvement in cloud height and motion arise due to a further increase of the amount of used ASI pairs (without adding additional ASIs).

The cloud modeling follows partly the 4Cam system as presented in 3.1, up to the point before the final shape correction of the cone like models. The final shape correction is done with the obtained height map. The 3-D coordinates of each cloudy voxel are compared with the 2-D coordinates of the orthogonal height map (see Figure 6). Voxels that match the height information of the height map remain marked as cloudy, other voxels are rejected. The following processing steps concerning the geometrical cloud thickness and allocation of cloud speed information are identical to the approach of the 2Cam system presented in section 3.2.

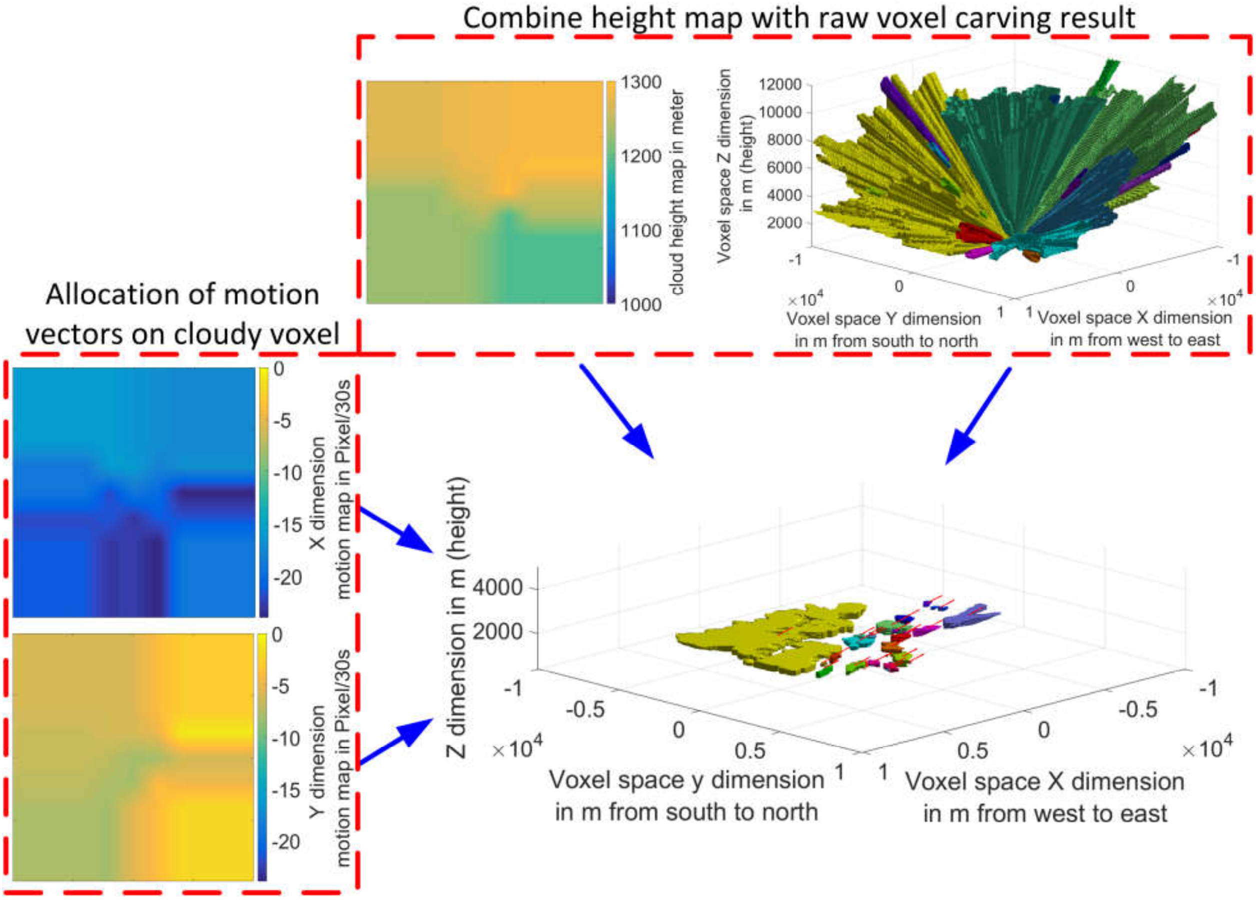

Figure 6: Shape correction of raw cloud models with cloud height map. Allocate speed vectors from 2-D orthogonal motion maps to cloudy voxel (each color represents an individual cloud model). (relevant for 4CamH)

4 Validation of cloud height and motion vectors

4.1 Cloud height validation of the three systems compared to a ceilometer

A 30 day period, distributed over the years 2015 and 2016, is used for the validation. The dataset is chosen in a way that a wide range of cloud heights, cloud motion patterns and atmospheric conditions are present.

Used error metrics include the MAE, relative MAE, RMSE and the relative RMSE. The absolute error metrics are calculated according to Equation 3 and Equation 4.

$$MAE = \frac{1}{n}\sum_{i=1}^{n}\left|Y_i - \hat{Y}_i\right| \qquad \textbf{Equation 3}$$

$$RMSE = \left[\frac{1}{n}\sum_{i=1}^{n}\left(Y_i - \hat{Y}_i\right)^2\right]^{0.5} \qquad \textbf{Equation 4}$$

Y_i is the reference value and $\hat{Y}_i$ the value derived from the ASI system. The relative error metrics are calculated from the absolute error metrics and the corresponding average reference value.

For the cloud height validation, cloud models are considered if their center is within 1 km from the vertical line marked by the ceilometers field of view. Ten-minute cloud height medians are calculated of all valid cloud models and from the ceilometer cloud height measurements. Timestamps are only considered for the evaluation, if the ceilometer and all involved ASI systems provide measurements. The average cloud heights as measured by the ceilometer and the corresponding number of measurements for different cloud height ranges are given in Table 2.

Table 2: Average cloud height and absolute number of measurements for reference ceilometer data

	0 m < h ≤ 3000 m	3000 m < h ≤ 6000 m	6000 m < h ≤ 9000 m	9000 m < h ≤ 12000 m	all
Average height	2001 m	3979 m	7676 m	10216 m	4089 m
Number of measurements	3752	3400	1308	566	9026

First, we have a closer look at three distinct days, one of them with simple single layer cumulus conditions and two with more complex multi-layer conditions including cumulus and cirrus clouds. Figure 7 illustrates the cloud height measurements for one day with predominant single layer clouds. On 19.9.2015 the ceilometer mainly measures cloud heights around 1600 m. Some clouds with a height around 2100 m appear after 16:00. The 2Cam and 4CamH systems show good alignment with the ceilometer measurements. A low relative MAE is reached for both new systems with 6.9% (2Cam) and 7.5% (4CamH) respectively. The 4Cam system shows larger fluctuations with strong outliers including deviations of various thousands of meters. The general trend of the cloud height is detected, but the relative MAE are significantly larger (16.0%).

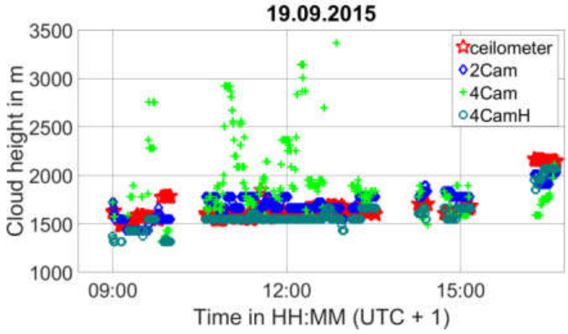

Figure 7: Measured cloud heights on 19.9.2015. Predominant single layer conditions are found around 1700 m.

Two days with more complex conditions are depicted in Figure 8. On 4.10.2015, two distinct layers are present. Often, the higher layer is blocked by the lower layer for the ceilometer as well as for the ASI systems. A short period from 10:23 to 10:30 with ceilometer measurements around 9600 m is completely ignored by the ASI systems, which only detect the lower layer. However, during the period from 12:40 to 12:57 the 2Cam and 4CamH systems detect mainly a higher predominant layer where the ceilometer measures a few small scattered clouds at the lower layer. For this period, in particular, the 4Cam system shows a good match with the ceilometer data. In general, 2Cam and 4CamH show more stable and accurate cloud height detections and an overall good match with a relative MAE of 28.8% and 23.8% compared to 4Cam with a relative MAE of 41.2%.

On 18.10.2015 three distinct layers are visible in the data shown in Figure 8. The 2Cam and 4CamH system follow the general trend of the ceilometer measurements. Higher deviations are present for the highest cloud layer, where the 2Cam and 4CamH systems often overestimate the cloud height. Especially 2Cam shows deviations up to 3000 m, during the time period 15:23 to 15:47. 4Cam follows the general trend as well, but with higher fluctuations. The overall relative MAE for this day is around 25.7% (2Cam) and 21.6% (4CamH) and around 29.9% for 4Cam.

The larger deviation observed for 4.10.2015 and 18.10.2015 are caused by complex multi-layer cloud conditions. Often higher layers are (partially) occluded by a lower layer. During these multi-layer scenarios, with a large cloud coverage of the lower layer, small gaps in the lower layer coverage allow ceilometer height measurements of higher layers. However, due to visual obstructions, the ASI systems often see mainly the lower layer. Multiple layers can only be detected by the ASI systems at the same time, if larger gaps are present in the lower cloud layers providing an unobstructed view.

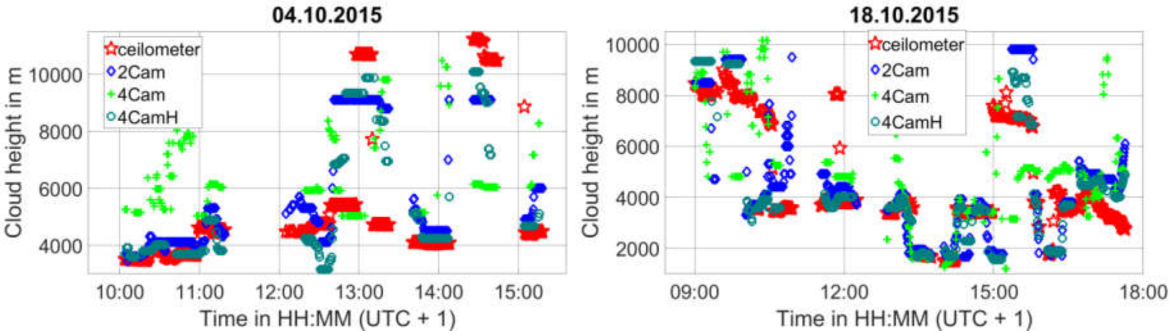

Figure 8: Measured cloud heights for all cloud modeling systems and reference ceilometer on 04.10.2015 and 18.10.2015. Both days show multiple cloud layers.

Figure 9 illustrates the histograms of the cloud heights obtained by the ceilometer and the three cloud modeling approaches for the complete 30-days data set. A strong mismatch can be seen for the 4Cam system compared to the ceilometer reference in the cloud height range below 2000 m with a frequency of 9% (ASI 4Cam) compared to 25% (ceilometer) and in the range between 5000 m to 6000 m with a frequency of 22% (ASI 4Cam) compared to 4% (ceilometer). Above 6000 m the match of the distribution is acceptable. For the 2Cam system, an overall good match is achieved for cloud heights up to 9000 m. Almost no clouds are detected above 10000 m. This is related to a systematic weakness of the approach caused by the available image resolution and camera distance, which will be discussed in section 4.1.2. The overall best match is achieved by the 4CamH system. No cloud height range shows strong deviations compared to the reference distribution, with the exception of a lack of measurements above 11000 m. The systematical weaknesses of the 2Cam system are also present for the 4CamH system, but less pronounced (see section 4.1.2).

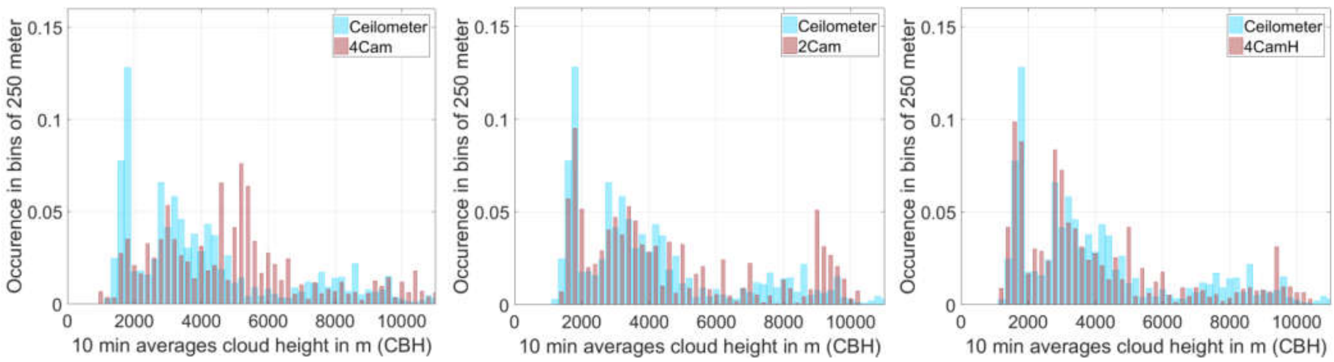

Figure 9: Histogram of the cloud heights obtained by the three cloud modeling approaches in comparison to the ceilometer measurements on 30-days

The comparison is also shown in scatter density plots (Figure 10). The reference ceilometer data are plotted on the abscissa and the ASI data on the ordinate. Each bin has a size of 250 m. The color coding represents the relative frequency for each pixel in a column of the scatter density plot. Accumulated relative frequencies of one column add up to 100%.

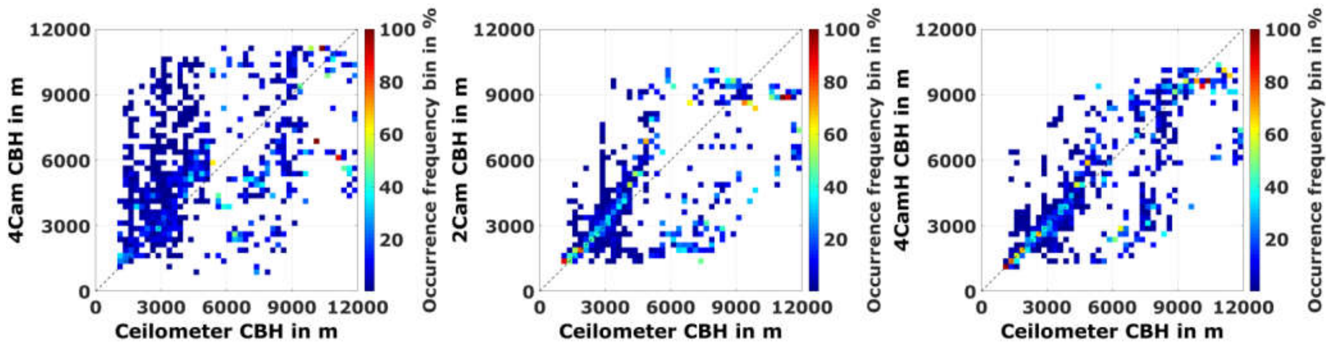

Figure10: scatter density plot of the cloud heights obtained by the three cloud modeling approaches in comparison to the ceilometer measurements on 30-days

The 4Cam system shows the largest dispersion and deviations, although up to around 5500 m the deviations are mostly below 500 m. A strong bias for higher clouds is seen in the range up to 5500 m. Dispersion and deviations increase farther for higher cloud layers. A negative bias can be seen for cloud heights above 5500 m, where the ceilometer detects high clouds but the ASI system detects low clouds. The latter effect can be seen for all three systems. This is due to the previously discussed multilayer conditions, with a strong cloud coverage of the lower layer, which blocks for most parts of the sky the higher layers. 2Cam and 4CamH show a better matching accuracy than the 4Cam system, especially for the lower cloud heights. We observe a positive offset for clouds higher than 4000 m. The offset increases with the cloud height. The effect is more pronounced for 2Cam and is due to the mentioned systematical issues which will be discussed in section 4.1.2.

Error metrics for distinct cloud height ranges are shown in Figure 11. As expected from the previous observation, the 4Cam system shows larger errors compared to 2Cam and 4CamH system. In the case of the 4Cam system, around 31% of all detected clouds received a substituted cloud height from a database, according to the procedure described in section 3.1.1. 4CamH has the lowest deviation of all systems. The relative MAE corresponding to the entire data set are 29% (2Cam), 17% (4CamH) and 46% (4Cam). One source for the observed deviation is, that all ASI systems measure an average cloud height and derive the CBH with an estimated cloud thickness. The ceilometer on the other hand measures directly the CBH.

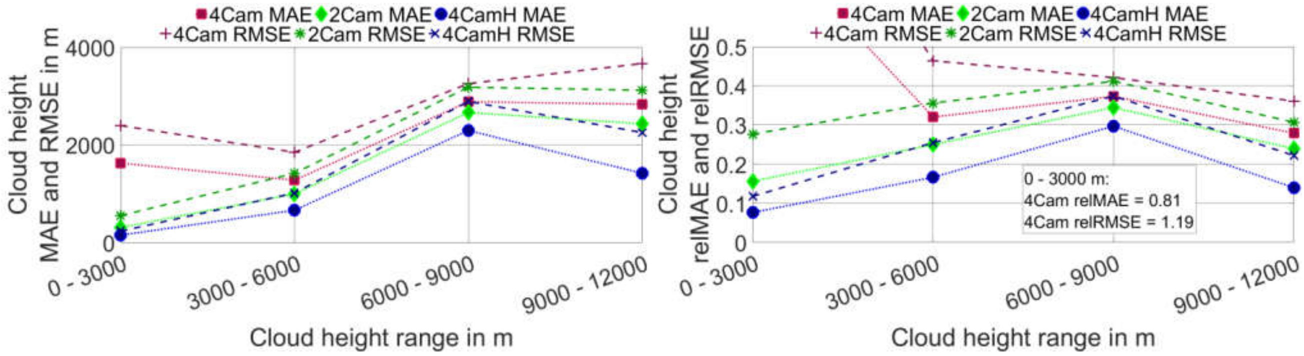

Figure 11: Resulting absolute (left) and relative (right) MAE and RMSE from the comparison of the ceilometer measurements discretized over cloud height ranges. The 4Cam relative MAE and RMSE for the lowest height range are given in the text field.

4.1.1 Understanding the deviations of the 4Cam approach

The 4Cam system identifies the cloud height of each cloud model individually by detecting the intersection of the field of views at the cloud edges. The cloud edges are located by the corresponding minimum and maximum pixel elevation angle of a vertical cloud model cross section (see Figure 13). An error estimation for resulting cloud heights and position of the observed cloud edges is conducted. This study considers two cameras with a distance of 700 m to each other. Hypothetical clouds are considered, with varying cloud edge height and horizontal distance to the point of origin. The point of origin is located between the cameras. The resulting pixel elevation angles are calculated with the known relative position of the cloud edges to the cameras. In a next step, errors are added to the calculated angles (e.g. error of +0.5°). The resulting position of the cloud edges can be calculated by the erroneous angles. Thus, the expected resulting cloud height and cloud edge position can be estimated. Real errors of the pixel elevation angle arise mainly due to not ideal ASI calibrations, ASI misalignments and segmentation errors.

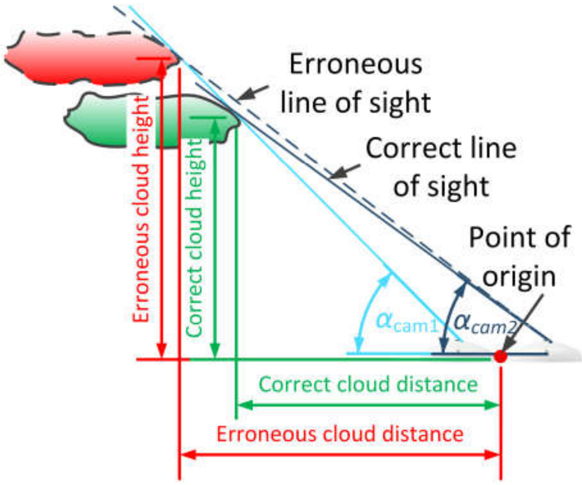

Figure 13: Correct and erroneous cloud edge position due to an pixel elevation angle error of +0.5° of cam2

Whether an erroneous lower (closer) or a higher (farther) cloud position is detected, depends on the direction of the angle error and the relative position of the corresponding camera to the second camera and the cloud. Thus, simultaneously occurring angle errors from multiple cameras can amplify or attenuate the effect.

Figure 14 illustrates the expected errors for cloud height (a) and cloud edge (b) positions and an erroneous pixel elevation angle of +0.5°. 0.5° corresponds to around five pixels in the west-east or south-north axis of the image. The correct distance between the point of origin and the cloud edge is shown on the abscissa and the cloud height on the ordinate. The color bar describes the resulting error of the cloud edge in height and distance respectively. For example, the errors for a cloud with a height of 6000 m and a distance of 10000 m are +1255 m (height) and +2165 m (distance). Expected errors increase for higher clouds or for clouds, which are farther away.

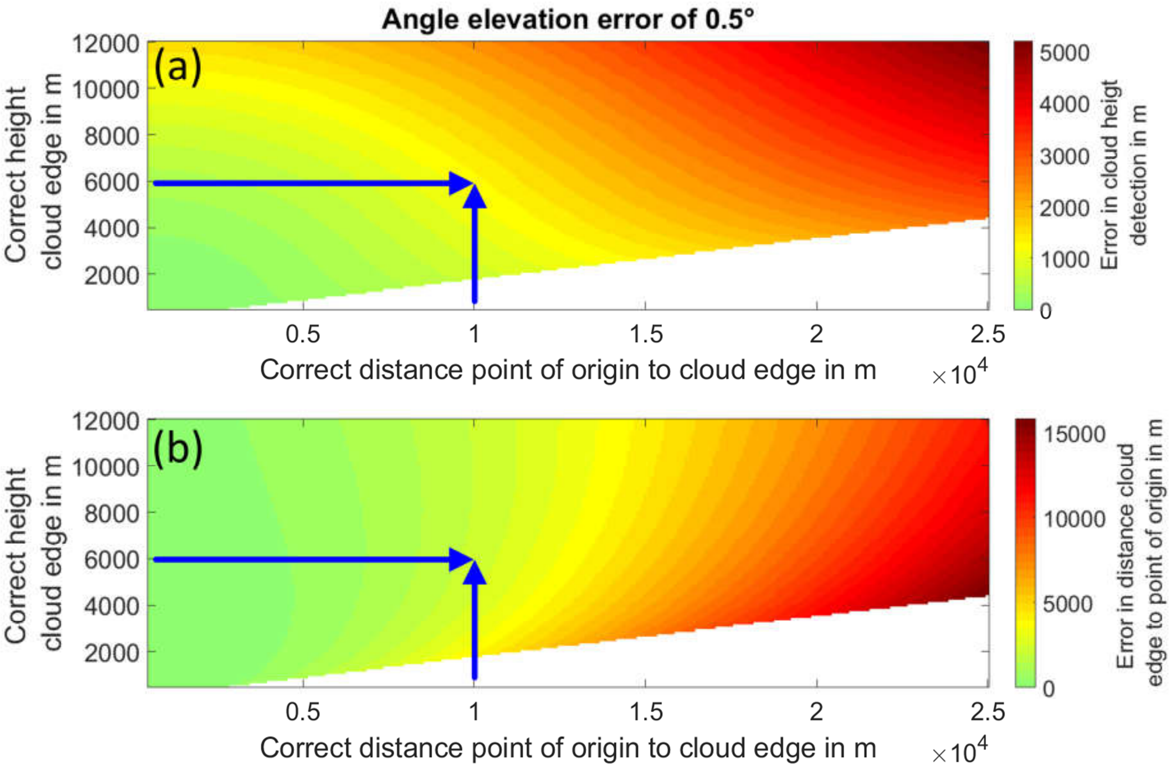

Figure 14: Expected errors in cloud height (a) and position (b) due to the erroneous pixel elevation angle of +0.5°. Arrows mark the described example.

It has to be pointed out, that four cameras amount to six distinct camera pairs and thus in six distinct cloud height measurements for the same cloud edge (see section 3.1). Averaging reduces the magnitude of the errors. Nevertheless, this analysis shows some weaknesses and physical limitations of the 4Cam system, especially for distant and high clouds.

4.1.2 Understanding the deviations of the 2Cam and 4CamH approach

As described in section 3.2, the 2Cam and 4CamH system uses a cross correlation approach by matching difference images from two ASIs. The maximum resolvable height depends on the image resolution and the distance between the ASIs. A larger distance between the ASIs will allow measuring the height of higher clouds, but reduces the capability for low clouds. An cloud has to be present in the image intersection of both ASIs. For clouds at a height close to the geometrical limitations of an ASI setup (correlation distance of only a few pixels), the height resolution is defined by very large increments. Therefore, the absolute uncertainties increase for such clouds (due to the limitations of the height resolution). This issue is even more pronounced if matching errors are taken into account.

As an example, two setups of ASIs are assumed, one with a distance between the ASIs of 470 m and the second with 950 m. Both setups work with orthogonal images using a maximum zenith angle of 78° and are projected into an orthoimage of 1000x1000 pixels. Both setups observe the same cloud roughly at 10000 m above the ASIs. This corresponds to a correlation distance of 5 pixels for the first setup and 10 for the second setup. A single pixel error of -1 pixel implies a higher cloud for both setups. The first setup would detect an cloud at a height of roughly 12500 m and the second setup would detect an cloud at a height of roughly 11200 m. A pixel error of +1 pixel results at a height of 8300 m (setup 1) and 9200 m (setup 2). Figure 15 (a) and (b) show different pixel correlation distances for different ASI setups. The color bar of Figure 15 (a) describes the correct cloud height, whereas the color bar of Figure 15 (b) describes the expected cloud height error due to a matching error of -1 pixel. The expected errors are below 100 m for most cases. A strong increase of the expected errors can be seen for all scenarios with a matching distance below 10 pixels. These systematic errors can result in unrealistic heights (>15000 m), especially in the case of absolute matching errors larger than -1 pixel. This issue is also present for positive pixel errors, but less influential. The increment in height per pixel drops rapidly for larger correlation distances.

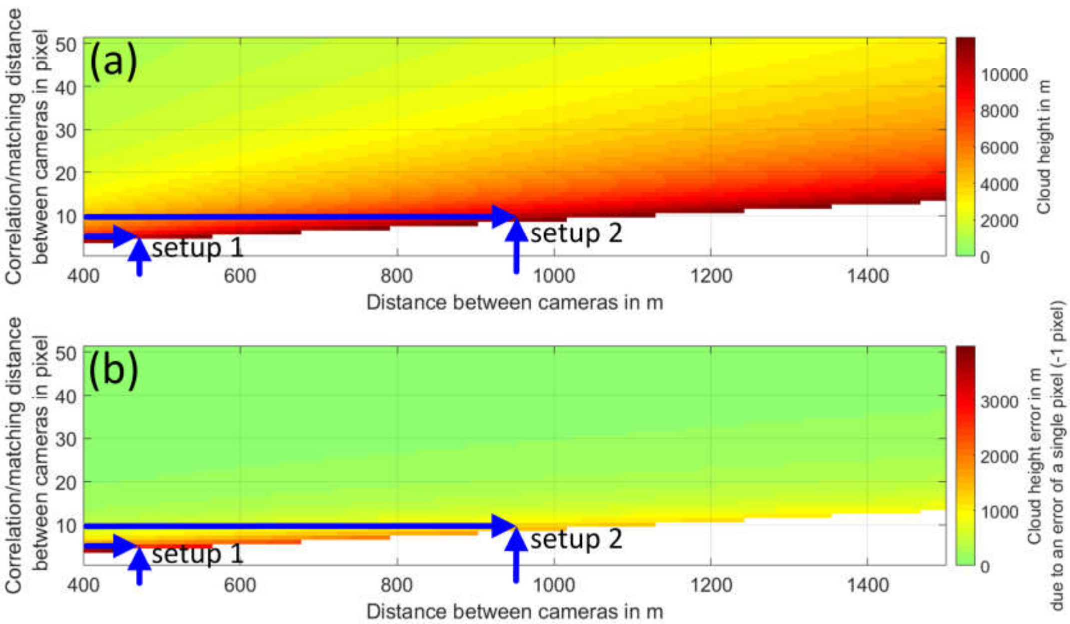

Figure 15: Expected errors in cloud height and position due to a matching error of -1 pixel for distinct ASI setups and corresponding matching results. Arrows mark the described example. a) Expected cloud height without errors (Cloud heights limited to 12000 m) b) Cloud height errors due to the matching errors

The 2Cam set up operated at the PSA with a camera distance of roughly 500 m is vulnerable to the described issue (see Figure 15). Unrealistic cloud heights (>>12000 m) are detected and substituted by an average cloud height from valid recent historical measurements (same day). If no valid historical cloud height information are available, we substitute the cloud height with an default value of 9000 m. This explains some of the deviations shown in Figure 9 and Figure 10 as well as the described gradually increasing offset seen in Figure 10.

Matching errors that lead to lower clouds are less pronounced and more difficult to detect, as realistic cloud heights are derived. This may partially explains the over-representation of lower ASI cloud heights for ceilometer readings above 6000 m (see Figure 10).

The 4CamH system is less prone to mismatches, as multiple camera pairs are used for the cloud height detection. Unrealistic cloud heights are rejected. Only in very rare cases show all used camera pairs simultaneously similar matching errors. In such cases, the described substitution process of the 2Cam system is applied.

4.2 Cloud motion vector validation of the three systems compared to shadow camera system

In this section, cloud motion vectors derived from three ASI configurations are benchmarked against a shadow camera system using 10-minute median values. Timestamps are considered, only if all involved systems provide a measurement.

The measured direction and speed of the reference system and all ASI systems is depicted in Figure 16. In general, all three ASI systems follow the direction as measured by the reference system. Similar results with an overall good match are reached for the cloud speed from the visual inspection in the case of 2Cam and 4CamH. 4Cam shows again stronger fluctuations and some persistent deviations.

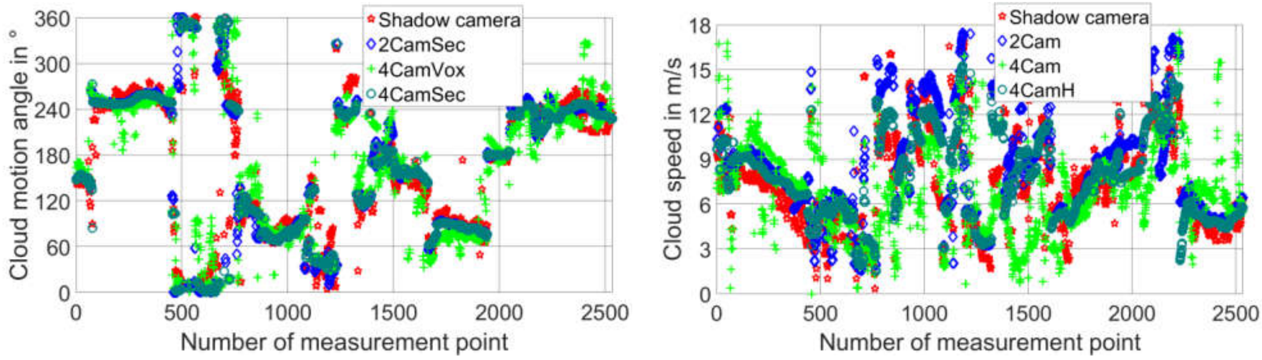

Figure 16: Motion direction (left) and speed (right) for the reference shadow cam and all three ASI systems over the entire data set.

The histograms illustrated in Figure 17, confirm the good agreement for the direction. The gap around 330° is related to the local main cloud directions at the site. Cloud movements roughly to the north are a considerable rare event above the PSA. Most clouds move on a west-east axis. Interestingly, the 4Cam cloud speed distribution shows the best match with the reference system, despite the strong fluctuations. However, this is only a statistical result, under consideration of the entire data set.

The 2Cam cloud speed distribution shows a lack of measurements in the 5 and 8 m/s bin, but this is compensated by an increased population within the neighboring bins. The 4CamH system shows an overall good agreement with the cloud speed distribution.

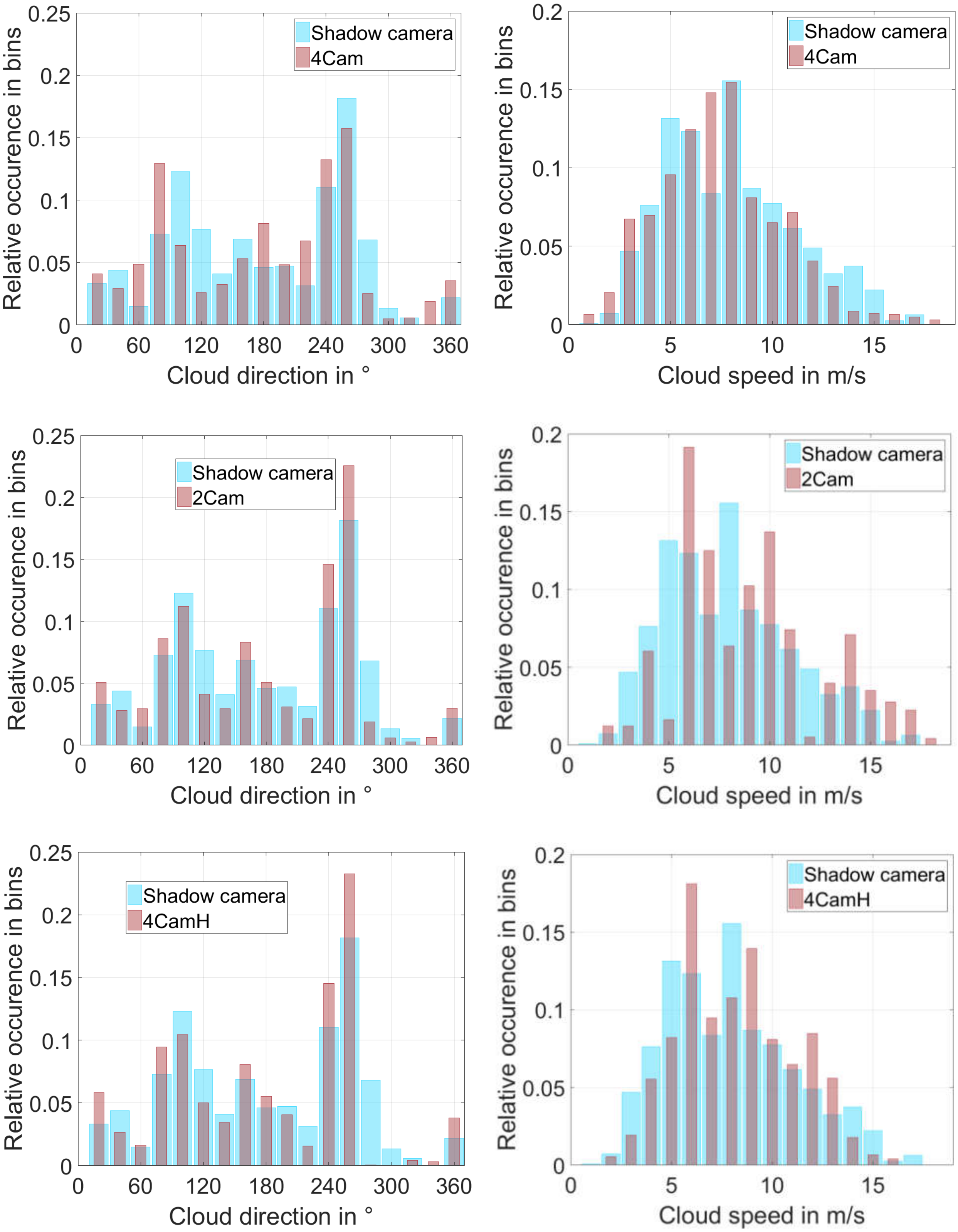

Figure 17: Histograms of reference and ASI systems; left: cloud motion direction (north: 0°, east: 90°, south: 180° and west: 270°) right: cloud speed

Scatter density plots for the direction and speed are depicted in Figure 18. All frequencies in one reference bin (column) add up to 100%. As expected, the 4Cam system shows the strongest dispersion for the direction as well for the speed. Overall, the scatter density plot confirms the good agreement off all systems for the motion direction with an MAE of 22.7° (4Cam), 12.8° (2Cam) and 11.7° (4CamH) (see Table 3).

Despite the low deviations of the speed distribution, the scatter density plot shows a poor alignment for the 4Cam system with an overall MAE of 2.6 m/s. An improvement can be seen for the 2Cam and especially for the 4CamH system with MAEs dropping to 1.8 m/s and 1.3 m/s respectively (see Table 3).

Table 3: Resulting MAE and RMSE from the comparison of the shadow camera system to the ASI systems over the entire range (v: cloud speed and β: cloud motion angle)

	4Cam		2Cam		4CamH	
MAE (v ≤ 18m/s)	2.6 m/s	34%	1.8 m/s	23%	1.3 m/s	18%
MAE (β ≤ 360°)	22.7 °	-	12.8 °	-	11.7 °	-
RMSE (v ≤ 18m/s)	3.3 m/s	43%	2.3 m/s	30%	1.7 m/s	23%
RMSE (β ≤ 360°)	29.2 °	-	17.4 °	-	16.2 °	-

The 2Cam and 4CamH show a minor bias towards higher velocities that increases for higher values. This can be explained partially by difficulties in detecting altitudes of high clouds. As shown in section 4.1.2, small matching errors for high clouds have a strong impact on the detected cloud height. Clouds erroneously estimated to be too high indicate larger pixel edge lengths in m, which leads to higher cloud speeds.

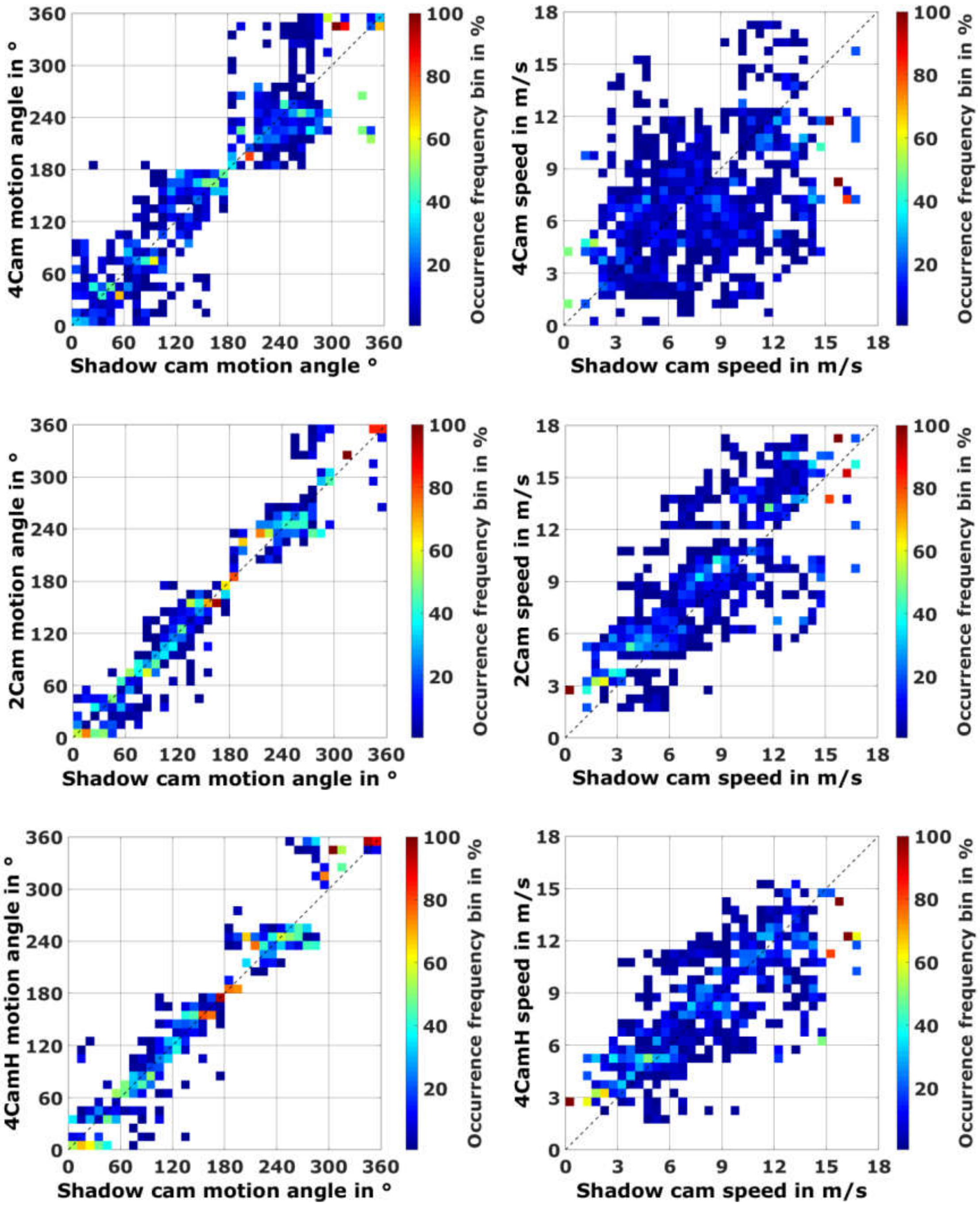

Figure 18: Scatter density plots of reference and ASI systems; On the left direction (north: 0°, east: 90°, south: 180° and west: 270°) and on the right speed

MAE and RMSE over different cloud speed ranges are depicted in Figure 19. An absolute increase of the errors can be seen for higher velocities. 4CamH is the most accurate system in all cloud speed ranges, followed by 2Cam and finally 4Cam.

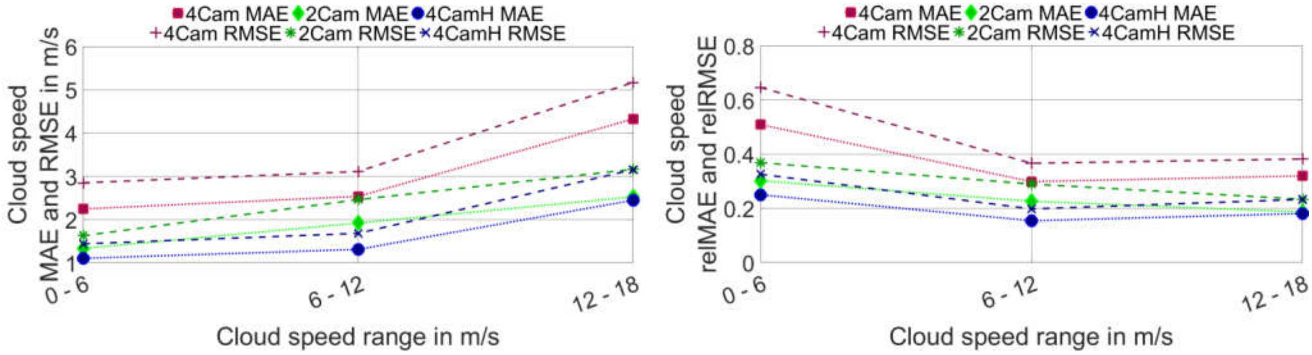

Figure 19: MAE and RMSE in comparison to the shadow camera system discretized over cloud speed ranges

One reason for the increased deviations of the 4Cam system, is the direct interaction with the height detection. As presented in section 4.1 the deviations for the height are the largest for the 4Cam system. The derived cloud height has a strong impact on the resulting size and shape of modeled clouds, which increases the possibilities of mismatches (see section 3.1).

For 2Cam and 4CamH, we use orthogonal images including zenith angle up to 78° described by 1000 pixel. This leads to resolution constraints. In the case of a hypothetical cloud at 12000 m, the pixel edge length corresponds to roughly 113 m/pixel. Thus, small matching errors for high clouds lead to large motion deviation, which partially explains the increased deviations for high velocities.

5 Discussion of results compared to previous findings

Comparisons between different systems is a complex task, as different systems are typically tested with different datasets from different sites. The accuracy of ASI systems depends heavily on the prevailing weather conditions. Single low layer cloud conditions with optical thick cumulus clouds represent conditions, where high accuracies are likely. High clouds pose a much tougher challenge, as we pointed out in section 4.1.1 and 4.1.2. This is an inherent problem of all stereoscopic approaches. High clouds are also more challenging for single ASI approaches, due to resolution constraints. Finally, complex but frequent multilayer cloud conditions (**Wang 2000**) represent challenges that are even more difficult. Nevertheless, we compared in **Kuhn et al. 2018** cloud heights derived with different ASI systems for a 59-day validation period, with an overall MAE of 872 m. In this work, we continue the comparison adding the three cloud model oriented ASI systems. Comparably good results are reached in the 30 day validation period with an overall MAE of 1145 m (2Cam) and 648 m (4CamH). The comparison must take into account that **Kuhn et al. 2018** is limited to a single cloud layer at any given time and rejects all times stamps surpassing a maximum cloud height threshold.

Intercomparison of the motion vectors is even more challenging. Most motion vector validation are done indirectly by comparing the achieved forecast score (**Quesada-Ruiz et al. 2014 and Peng et al. 2015**) or by comparing the previously forecasted cloud cover with the corresponding real cloud cover (**Huang et al. 2012, Chow et al. 2015 and Zaher et al. 2017**). Others estimate motion vector uncertainties (**Crispel et al. 2017 and Schmidt et al. 2016**).

6 Conclusion and outlook

We developed two novel cloud model oriented ASI based nowcasting systems, which use individual cloud models with individual attributes such as height, position, surface area, volume, transmittance, motion vector. Our 2Cam system is a further development of a previously published two ASI based cloud height detection and cloud tracking approach independent of the cloud segmentation (**Kuhn et al. 2018**). The 4CamH system is a hybridized approach that combines a previously published 4Cam voxel carving approach (**Nouri et al. 2017**) with the novel 2Cam system. In this work, we compared the three cloud model oriented systems in terms of cloud height detection accuracy with a ceilometer and the cloud tracking accuracy with a shadow camera system.

Our 30 day validation period showed the strongest deviation both for height detection and cloud tracking with the 4Cam system. The 4Cam system reached an overall MAE of 1793 m for the height, 2.6 m/s for the cloud speed and 22.7° for the motion direction. The 2Cam and 4CamH systems showed better results, with overall MAE of 1145 m (2Cam) and 648 m (4CamH) for the height, 1.8 m/s (2Cam) and 1.3 m/s (4CamH) for the speed and 17.4° (2Cam) and 16.2° (4CamH) for the direction. The comparison between the two voxel carving approaches (4Cam and 4CamH), emphasized the impact of error propagation effects of previous processing steps (e.g. cloud segmentation uncertainties). Especially the 4Cam cloud tracking was penalized by erroneous cloud heights, which lead to shape and size changes of the clouds.

4CamH outperformed 2Cam by combining the robust voxel carving approach for the cloud modeling with height and motion maps developed for 2Cam. Further reductions of the uncertainties were achieved by averaging height and motion maps from four distinct ASI pairs.

The advantages of 2Cam are lower hardware and maintenance costs and a less CPU-intensive image processing. Furthermore, the lower computing requirements of the 2Cam approach, allow a higher temporal resolution, considering the same computing capacities.

We studied some inherent systematical weaknesses of ASI based nowcasting systems, in the case of high altitude clouds, and described some strategies to reduce the impact on the system accuracy. These strategies are limited to the 2Cam and 4CamH approach and incorporate valid recent historical cloud height measurements which substitute clearly invalid cloud height information's with cloud heights >>12000 m. These weaknesses were mainly caused by the geometrical setup of the ASIs and the image resolution. A hardware upgrade consisting of cameras with a higher image resolution would reduce the impact of these effects. The drawbacks are an increased computation time.

All three systems are real-time capable with a time resolution of 30 s and produce spatial irradiance forecast up to 15 minutes ahead (in one minute increments) for an area up to 64 km^2 and a spatial resolution down to 5 m.

The main target applications of our ASI based nowcasting systems are optimized CSP plant operation (**Noureldin et al. 2017**), PV-battery operation (**Kuhn et al. 2017a**) and optimization of electricity grid operations (**Perez et al. 2016**). An additional application is the usage of ASIs as a standardized sensor for automated meteorological stations (e.g. for cloud coverage and cloud classification).

Acknowledgment

The German Federal Ministry for Economic Affairs and Energy funded the presented research within the WobaS project.

Thanks to the colleagues from the Solar Concentrating Systems Unit of CIEMAT for the support provided in the installation and maintenance of the shadow cameras. These instruments are installed on CIEMAT's CESA-I tower of the Plataforma Solar de Almería.

References

Allmen, M.C., Kegelmeyer Jr., W.P., 1996. The computation of cloud-base height from paired whole-sky imaging cameras. J. Atmos. Ocean. Technol. 13 (1), 97–113. http://journals.ametsoc.org/doi/abs/10.1175/1520-0426(1996)013%3C0097:TCOCBH%3E2.0.CO%3B2 .

Beekmans, C., Schneider, J., Läbe, T., Lennefer, M., Stachniss, C., Simmer, C., 2016. Cloud photogrammetry with dense stereo for fisheye cameras. Atmos. Chem. Phys. 16 (22), 14231–14248. http://dx.doi.org/10.5194/acp-16-14231-2016.

Blanc, P., Massip, P., Kazantzidis, A., Tzoumanikas, P., Kuhn, P., Wilbert, S., Schüler, D., Prahl, C., 2017. Short-term forecasting of high resolution local DNI maps with multiple fish-eye cameras in stereoscopic mode. AIP Conf. Proc. 1850 (1), 140004.. http://aip.scitation.org/doi/abs/10.1063/1.4984512.

Blanc, P., Remund, J., Vallance, L., 2017. Short-term solar power forecasting based on satellite images. Renewable Energy Forecasting, 179–198. doi:10.1016/b978-0-08-100504-0.00006-8

Bone, V., Pidgeon, J., Kearney, M., Veeraragavan, A., 2018. Intra-hour direct normal irradiance forecasting through adaptive clear-sky modelling and cloud tracking. Solar Energy 159, 852–867. https://doi.org/10.1016/j.solener.2017.10.037

Bosch, J.L., Kleissl, J., 2013. Cloud motion vectors from a network of ground sensors in a solar power plant. Solar Energy 95, 13-20. https://doi.org/10.1016/j.solener.2013.05.027

Bright, J. M., Killinger, S., Lingfors, D., & Engerer, N. A., 2018. Improved satellite-derived PV power nowcasting using real-time power data from reference PV systems. Solar Energy, 168, 118–139. doi:10.1016/j.solener.2017.10.091

Calbó, J., Long C.N., González, J-A., Augustine, J., McComiskey, A., 2017, The thin border between cloud and aerosol: Sensitivity of several ground based observation techniques, Atmos. Res. 196, 248–260. http://dx.doi.org/10.1016/j.atmosres.2017.06.010

Chow, C.W., Urquhart, B., Lave, M., Dominguez, A., Kleissl, J., Shields, J., Washom, B., 2011. Intra-hour forecasting with a total sky imager at the UC San Diego solar energy testbed. Solar Energy 85, 2881–2893. http://dx.doi.org/10.1016/j.solener.2011.08. 025.

Chow, C.W., Belongie, S., Kleissl, J., 2015. Cloud motion and stability estimation for intra-hour solar forecasting. Solar Energy 115, 645–655. http://dx.doi.org/10.1016/j.solener.2015.03.030.

Crispel, P., Roberts, G., 2017. All-sky photogrammetry techniques to georeference a cloud field. Atmos. Meas. Tech., 11, 593–609. https://doi.org/10.5194/amt-11-593-2018

Farnebäck, G., 2003. Two-frame motion estimation based on polynomial expansion. Image Anal., 10, 363–370. DOI:10.1007/3-540-45103-X_50

Fung, V., Bosch, J.L., Roberts, S.W., Kleissl, J., 2013. Cloud shadow speed sensor. Atmos. Meas. Techn. 6 (5). http://dx.doi.org/10.5194/amt-7-1693-2014.

Huang, H., Yoo, S., Yu, D., Huang, D., Qin, H., 2012. Correlation and local feature based cloud motion estimation. In: Proceedings of the Twelfth International Workshop on Multimedia Data Mining. MDMKDD ’12. ACM, New York, NY, USA, pp. 1–9. http://doi.acm.org/10.1145/2343862.2343863 .

Inman, R.H., Pedro, H.T.C., Coimbra, C.F.M., 2013. Solar forecasting methods for renewable energy integration. Prog. Energy Combust. Sci. 39, 535–576. http://dx.doi.org/10.1016/j.pecs.2013.06.002.

Kahn, B.H., Chahine, M.T., Stephens, G.L., Mace, G.G., Marchand, R.T., Wang, Z., Barnet, C.D., Eldering, A., Holz, R.E., Kuehn, R.E., Vane, D.G., 2008. Cloud type comparisons of

AIRS, CloudSat, and CALIPSO cloud height and amount, Atmos. Chem. Phys., 8, 1231-1248, https://doi.org/10.5194/acp-8-1231-2008.

Kalman, R.E., 1960. A New Approach to Linear Filtering and Prediction Problems. J. Basic Eng. 82. 35-45. doi:10.1115/1.3662552

Kassianov, E., Long, C.N., Christy, J., 2005. Cloud-base-height estimation from paired ground-based hemispherical observations. J. Appl. Meteorol. 44 (8), 1221–1233. http://dx.doi.org/10.1175/JAM2277.1.

Kazantzidis, A., Tzoumanikas, P., Blanc, P., Massip, P., Wilbert, S., Ramirez-Santigosa, L., 2017. 5 - short-term forecasting based on all-sky cameras. In: Kariniotakis, G. (Ed.), Renewable Energy Forecasting. Woodhead Publishing Series in Energy. Woodhead Publishing, pp. 153–178. http://www.sciencedirect.com/science/article/pii/B9780081005040000056

Kuhn, P., Nouri, B., Wilbert, S., Prahl, C., Kozonek, N., Schmidt, T., Yasser, Z., Ramirez, L., Zarzalejo, L., Meyer, A., Vuilleumier, L., Heinemann, D., Blanc, P., Pitz-Paal, R., 2017a. Validation of an all-sky imager-based nowcasting system for industrial PV plants. Prog. Photovolt.: Res. Appl. http://dx.doi.org/10.1002/pip.2968.

Kuhn, P., Wirtz, M., Wilbert, S., Bosch, J., Heinemann, D., Kleissl, J., Pitz-Paal, R., 2017b. Field validation and bechmarking of a cloud shadow speed sensor. Sol. Energy 173, 229–245. https://doi.org/10.1016/j.solener.2018.07.053

Kuhn, P., Wirtz, M., Killius, N., Wilbert, S., Bosch, J.L., Hanrieder, N., Nouri, B., Kleissle, J., Ramirez, L., Schroedter-Homscheidt, M., Heinemann, D., Kazantzidis, A., Blanc, P., Pitz-Paal, R., 2018. Benchmarking three low-cost, low-maintenance cloud height measurement systems and ECMWF cloud heights. Sol. Energy 168, 140–152. https://doi.org/10.1016/j.solener.2018.02.050

Kutulakos, K.N., Seitz, S.M., 2000. A theory of shape by space carving. International Journal of Computer Vision 38, 199–218. https://doi.org/10.1023/A:100819122

Lorenz, E., Remund, J., Müller, S., Traunmüller, W., Steinmaurer, G., Pozo, D., Ruiz-Arias, J., Fanego, V., Ramirez, L., Romeo, M., Kurz, C., Pomares, L., Guerrero, C., 2009.

Benchmarking of different approaches to forecast solar irradiance. 24th European Photovoltaic Solar Energy Conference, Hamburg, Germany, 21–25.

Luhmann, T., 2003. Nahbereichsphotogrammetrie: Grundlagen, Methoden und Anwendungen. 2. Auflage, Herbert Wichmann Verlag, Heidelberg

Martucci, G., Milroy, C., O’Dowd, C.D., 2010. Detection of cloud-base height using Jenoptik CHM15K and Vaisala CL31 ceilometers. J. Atmos. Ocean. Technol. 27 (2), 305–318. http://dx.doi.org/10.1175/2009JTECHA1326.1.

Menzel, W.P., Smith, W.L., Stewart, T. R., 1983. Improved cloudmotion wind vector and altitude assignment using VAS, J. Climate Appl.Meteorol., 22, 377–384. https://doi.org/10.1175/1520-0450

Moran, K.P., Martner, B.E., Post, M.J., Kropfli, R.A., Welsh, D.C., Widener, K.B., 1998. An unattended cloud-profiling radar for use in climate research. Bull. Amer. Meteor. Soc., 79, 443– 455. https://doi.org/10.1175/1520-0477

Nguyen, D.A., Kleissl, J., 2014. Stereographic methods for cloud base height determination using two sky imagers. Solar Energy 107, 495–509. http://dx.doi.org/10.1016/j.solener.2014.05.005.

Nieman, S.J., Schmetz, J., Menzel, W.P., 1993. A comparison of several techniques to assign heights to cloud tracers. Appl. Meteor., 32, 1559-1568. https://doi.org/10.1175/1520-0450

Noh, Y., Forsythe, J., Miller, S., Seaman, C., 2017. Cloud-base height estimation from VIIRS. Part II: A statistical algorithm based on A-Train satellite data. J. Atmos. Oceanic., 34, 585–598, doi:10.1175/JTECH-D-16-0110.1.

Noureldin, K., Hirsch, T., Pitz-Paal, R., 2017. Virtual Solar Field - Validation of a detailed transient simulation tool for line focus STE fields with single phase heat transfer fluid Sol. Energy 146, 131-140. https://doi.org/10.1016/j.solener.2017.02.028

Nouri B., Kuhn, P., Wilbert, S., Prahl, C., Pitz-Paal, R., Blanc, P., Schmidt, T., Yasser, Z., Ramirez Santigosa, L., Heineman, D., 2017. Nowcasting of DNI Maps for the Solar Field Based on Voxel Carving and Individual 3D Cloud Objects from All Sky Images, 23rd SolarPACES Conference

Peng, Z., Yu, D., Huang, D., Heiser, J., Yoo, S., Kalb, P., 2015. 3D cloud detection and tracking system for solar forecast using multiple sky imagers Sol. Energy 118, 496-519. https://doi.org/10.1016/j.solener.2015.05.037

Perez, R., David, M., Hoff, T.E., Jamaly, M., Kivalov, S., Kleissl, J., Lauret, P., Perez, M., 2016. Spatial and temporal variability of solar energy. Found. Trends Renew. Energy 1 (1), 1–44. http://dx.doi.org/10.1561/2700000006

Quesada-Ruiz, S., Chu, Y., Tovar-Pescador, J., Pedro, H., Coimbra, C., 2014. Cloud tracking methodology for intra-hour DNI forecasting. Solar Energy 102, 267–275. https://doi.org/10.1016/j.solener.2014.01.030.

Richardson, W., Krishnaswami, H., Vega, R., Cervantes, M., 2017. A Low Cost, Edge Computing, All-Sky Imager for Cloud Tracking and Intra-Hour Irradiance Forecasting. *Sustainability* 2017. *9*(4). 482. https://doi.org/10.3390/su9040482

Rossow, W. B., Schiffer, R. A., 1999. Advances in understanding clouds from ISCCP. Bull. Amer. Meteor. Soc., 80, 2261-2287. doi: 10.1175/1520-0477(1999)080<2261:AIUCFI>2.0.CO;2

Sassen, K., 1991. The polarization lidar technique for cloud research: A review and current assessment. Bull. Amer. Meteor. Soc., 72, 1848–1866. https://doi.org/10.1175/1520-0477

Scaramuzza, D., Martinelli, A., Siegwart, R., 2006. A toolbox for easily calibrating omnidirectional cameras. In: 2006 IEEE/RSJ International Conference on Intelligent Robots and Systems. IEEE, pp. 5695–5701.. <http://ieeexplore.ieee.org/abstract/ document/4059340/> .

Schmidt, T., Kalisch, J., Lorenz, E., Heinemann, D., 2016. Evaluating the spatio-temporal performance of sky-imager-based solar irradiance analysis and forecasts. Atmos. Chem. Phys. 16, 3399–3412. http://dx.doi.org/10.5194/acp-16-3399-2016.

Schroedter-Homscheidt, M., Gesell, G., 2016. Verification of sectoral cloud motion based direct normal irradiance nowcasting from satellite imagery, AIP Conf. Proc. 1734, 150007 https://doi.org/10.1063/1.4949239

Seiz, G., Shields, J., Feister, U., Baltsavias, E., Gruen, A., 2007. Cloud mapping with ground-based photogrammetric cameras. Int. J. Remote Sens. 28 (9), 2001–2032. http://dx.doi.org/10.1080/01431160600641822.

Venema, V., Russchenberg, H., Apituley, A., Lammeren, A., Ligthart, L., 2000. Cloud boundary height measurements using lidar and radar. Phys. Chem. Earth, 25B, 129–134, doi:10.1016/S1464-1909(99)00139-2.

Wang, J., Rossow, W., Zhang, Y., 2000. Cloud Vertical Structure and Its Variations from a 20-Yr Global Rawinsonde Dataset. J. Clim. 13, 3041 – 3056, https://doi.org/10.1175/1520-0442(2000)013<3041:CVSAIV>2.0.CO;2

Wang, G., Kurtz, B., Kleissl, J., 2016. Cloud base height from sky imager and cloud speed sensor. Sol. Energy 131, 208–221. http://dx.doi.org/10.1016/j.solener.2016.02.027.

Wang, Z., K. Sassen, 2001. Cloud type and macrophysical property retrieval using multiple remote sensors. Appl. Meteor., 40, 1665-1682. https://doi.org/10.1175/1520-0450.

West, SR., Rowe, D., Sayeef, S., Berry, A., 2014. Short-term irradiance forecasting using skycams: motivation and development. Sol. Energy. 110. 188-207. http://dx.doi.org/10.1016/j.solener.2014.08.038.

Wilbert, S., Nouri, B., Prahl, C., Garcia, G., Ramirez, L., Zarzalejo, L., Valenzuela, L., Ferrera, F., Kozonek, N., Liria, J., 2016. Application of Whole Sky Imagers for Data Selection for Radiometer Calibration. In: EU PVSEC 2016 Proceedings (2016), 1493–1498. http://dx.doi.org/10.4229/EUPVSEC20162016-5AO.8.6

Zaher, A., Thil, S., Nou, J., 2017. Comparative study of algorithms for cloud motion estimation using sky-imaging data. IFAC-PapersOnLine ;50:6108–13. http://dx.doi.org/10.1016/j.ifacol.2017.08.1488.